A data assimilation model for turbulent flows using continuous adjoint formulation

Chuangxin He, Yingzheng Liu, and Lian Gan

Citation: Physics of Fluids **30**, 105108 (2018); doi: 10.1063/1.5048727
View online: https://doi.org/10.1063/1.5048727
View Table of Contents: http://aip.scitation.org/toc/phf/30/10
Published by the American Institute of Physics

A data assimilation model for turbulent flows using continuous adjoint formulation

Chuangxin He,[1,2,3] Yingzheng Liu,[1,2,a)] and Lian Gan[3]
[1]*Key Lab of Education Ministry for Power Machinery and Engineering, School of Mechanical Engineering, Shanghai Jiao Tong University, 800 Dongchuan Road, Shanghai 200240, China*
[2]*Gas Turbine Research Institute, Shanghai Jiao Tong University, 800 Dongchuan Road, Shanghai 200240, China*
[3]*Department of Engineering, Durham University, Stockton Road, Durham DH1 3LE, United Kingdom*

(Received 17 July 2018; accepted 6 October 2018; published online 25 October 2018)

A generalized data assimilation model for turbulent flows using the continuous adjoint formulation is proposed. Within this formulation, the Spalart–Allmaras turbulence model is modified by adding a correction function β as a spatially varying coefficient to the turbulence production term. The model-form error is thus corrected by optimizing the β distribution, using the adjoint equations and the corresponding boundary conditions, to minimize the discrepancy between the predictions and observations. In addition, a constraint is applied to drive β toward a large value to avoid the flow unsteadiness owing to the low eddy viscosity. The present adjoint-based data assimilation (ABDA) model is expected to be applicable to various flow conditions unsolvable by the simple optimization of the model constant. This model is fully equation-driven and is thus computationally cheaper than the discretized adjoint method, as well as convenient to be implemented in the existing computational fluid dynamics codes. The flow over a cylinder with synthetic observations, the free round jet, the flow over a hump, and the three-dimensional flow over a wall-mounted cube, all of which are challenging for original Reynolds-averaged Navier–Stokes simulations, are employed to successfully demonstrate the reliability and capacity of the present ABDA model. The first-order scheme applied to the adjoint equations exhibits little effects on the final assimilation results, but improves the robustness significantly, and drives β to another solution that can also minimize the cost function. The present ABDA model is efficient in the heavy assimilation work of different types of shear and separated flows. *Published by AIP Publishing.* https://doi.org/10.1063/1.5048727

I. INTRODUCTION

The fast development of computational fluid dynamics (CFD) and measurement technologies is still primarily challenged by the accurate and complete determination of turbulent flows. The computationally cheap Reynolds-averaged Navier–Stokes (RANS) modeling typically generates strongly model-dependent flow information, far from being universal for widespread utilization;[1] meanwhile, the direct numerical simulation (DNS) and large-eddy simulation (LES) are prohibited in industry applications owing to the extremely heavy workload. State-of-the-art measurement techniques such as time-resolved tomographic particle image velocimetry (PIV) enables the determination of the spatio-temporal variation of three-dimensional velocity fields; however, a trade-off decision has to be made in terms of the factors among the temporal/spatial resolutions, the flow's physical domain, and the hardware performances. Nevertheless, the data assimilation (DA)[2] technique, which integrates the local measurement data (observations) and numerical modeling, could augment the turbulence model prediction beyond the spatially limited local measurements, yielding accurate flow reproduction in the global flow field. Undoubtedly, the development of an efficient DA model for turbulent flows is highly desirable.

DA is a mathematical technique that is initially developed in numerical weather prediction.[3] It helps us to gather the observation data at a given time and uses the equations of the flow dynamics and thermodynamics to estimate the future atmospheric state. From the last decade, DA has been sought for turbulence prediction by augmenting the numerical model with local observations. Among these studies, recalibrating the RANS model constants according to the flow information, using either a perturbation-based adaptation[4] or a statistical approach with an ensemble Kalman filter (EnKF),[5] has yielded significant improvements in the model performance. The former method calculates the approximate gradients of the cost function numerically by perturbing each model constant separately and adjusts them in the descending direction, whereas the latter determines an optimal set of model constants using the EnKF from a large ensemble, which is obtained by precursor simulations with random constant combinations (the same approach was also used by Gao *et al.*[6] for optimizing other model parameters). Both methods rely on a large number of tentative simulations, thus complicating the implementation process and increasing the computational cost. Moreover, the models might be formally wrong owing to the specific structure of the equations,[7] which would frustrate the determination

a)Author to whom correspondence should be addressed: yzliu@sjtu.edu.cn

of a suitable constant combination even when any of the recalibration procedures is used. In this regard, Oliver and Moser[8,9] induced a stochastic extension to the Boussinesq hypothesis based on Bayesian statistics, aiming at estimating the misfit of the RANS model to a set of observations. Unfortunately, the choice of stochastic extension and the dependency on the relevant observations still remain critical. Xiao *et al.*[10] introduced uncertainty terms directly into the Reynolds stresses to remedy the model-form error in a RANS simulation, with parameters determined iteratively using the EnKF. As declared by the authors, however, the inferred Reynolds stress field was inaccurate although this approach was not computationally intensive. Recently, the adjoint-based method has been introduced in field inversion,[11–13] in which a machine-learning scheme is proposed to augment the performance of the RANS model. This determines the parameters by calculating the gradients of the cost function directly using the adjoint system without any perturbation and tentative simulation; the model-form error of the RANS simulation can thus be eliminated by introducing a spatially distributed correction function into the model equation. Although only simple exemplary cases on prediction of the pressure coefficient have been presented, these present broad prospects in the data assimilation of turbulent flow fields.

The abovementioned efforts have primarily employed two approaches for the model-form correction of the RANS simulation, i.e., EnKF (or similar Bayesian statistics) and the adjoint-based method. The EnKF consists of serial propagation equations that are difficult to obtain explicitly in turbulent flows. This leads to a statistical data-driving approach for the determination of the Kalman gain, and the variance using a large ensemble that is computationally expensive for high-dimension systems,[14] or the inclusion of reduced-order models but with the introduction of extra model uncertainties.[15] The adjoint-based method is typically implemented in the discrete form, within which the system is discretized before the need of adjoint equation derivation. The choice of the discrete form is primarily due to the difficulties in the derivation of the adjoint equations and the embedding of the objective functions when otherwise implemented in the continuous form. However, the discrete adjoint method relies on the matrix operation that requires large memory,[16] thus restricting its use mostly in two dimensional flows.[11–13] The continuous adjoint method, on the contrary, is solely equation driven with a set of additional adjoint equations, and the corresponding boundary conditions complemented to the primal equation set. This requires a lower computational cost and can be easily implemented in the existing CFD codes, as reported in topology optimization.[17]

The present study concentrates on the development of a generalized adjoint-based data assimilation (ABDA) model for the reproduction of the global turbulent flow fields from the local measurement data. A full set of adjoint equations and the corresponding boundary conditions are derived, coupled with the primal Navier–Stokes (N–S) equations and the Spalart–Allmaras (SA) turbulence model.[18] The model-form error is corrected by a spatially distributed correction function that is determined using the measured wall pressure distribution or the local flow velocity as observations. This ABDA model is implemented in the open-source code, OpenFOAM (http://openfoam.org). The flow over a cylinder with synthetic observations, the free round jet[19] (free-shear flow), the flow over a hump[20,21] (separation from a smooth surface), and the full 3D flow over a wall-mounted cube[22] (3D flow with multiple separations and reattachments), all of which are challenging for original RANS simulations, are employed to successfully demonstrate the reliability and capacity of the present ABDA model.

II. MATHEMATICAL FORMULATIONS

A. RANS fundamentals and correction

The present ABDA formulation is derived from the time-independent SA model,[18] in which the turbulent eddy viscosity ν_t is determined

$$U_j \frac{\tilde{\nu}}{x_j} = P(\tilde{\nu}, \boldsymbol{U}) - D(\tilde{\nu}, \boldsymbol{U}) + T(\tilde{\nu}, \boldsymbol{U}), \tag{1}$$

where $\boldsymbol{U}$ represents the Reynolds-averaged fluid velocity; $P(\tilde{\nu}, \boldsymbol{U})$, $D(\tilde{\nu}, \boldsymbol{U})$, and $T(\tilde{\nu}, \boldsymbol{U})$ represent the production, dissipation, and transport of the turbulence quantity $\tilde{\nu}$, respectively, which are expressed as

$$P(\tilde{\nu}, \boldsymbol{U}) = C_{b1}\tilde{S}\tilde{\nu}, \tag{2a}$$

$$D(\tilde{\nu}, \boldsymbol{U}) = C_{w1} f_w \left(\frac{\tilde{\nu}}{d_w}\right)^2, \tag{2b}$$

$$T(\tilde{\nu}, \boldsymbol{U}) = \frac{\partial}{\partial x_j}\left[\left(\frac{\tilde{\nu}}{\sigma_{\nu t}} + \frac{\nu}{\sigma_{\nu t}}\right)\frac{\partial \tilde{\nu}}{\partial x_j}\right] + \frac{C_{b2}}{\sigma_{\nu t}}\left(\frac{\partial \tilde{\nu}}{\partial x_j}\right)^2. \tag{2c}$$

The turbulent eddy viscosity is determined by

$$\nu_t = f_{\nu 1}\tilde{\nu}. \tag{3}$$

The definitions of other quantities and the values of the model constants involved in Eqs. (2) and (3), which can be found in Ref. 18, are not shown here for clarity. However, the major source of the modeling error is the structure of the model equation [Eq. (1)] rather than the model constants. Accordingly, the reformulation of the model equation is necessary for the accurate prediction of the turbulent flows.

The basic idea of the ABDA model is to construct a spatially distributed function $\beta(\boldsymbol{x})$ imposed on the production term to correct the model-form error.[12] The modified SA model thus becomes

$$U_j \frac{\tilde{\nu}}{x_j} = \beta(\boldsymbol{x})P(\tilde{\nu}, \boldsymbol{U}) - D(\tilde{\nu}, \boldsymbol{U}) + T(\tilde{\nu}, \boldsymbol{U}). \tag{4}$$

The dimensionless correction function $\beta(\boldsymbol{x})$ changes the entire balance of the equation when it deviates from unity. Indeed, the correcting function can be added on other terms or introduced as a source term in Eq. (1). However, the current formulation is typically adopted in the field inversion problem owing to the convenience in implementation.[11–13]

B. Derivation of the adjoint system

Following the idea of the adjoint-based topology optimization,[17] the present DA can be achieved by minimizing

the cost function $\mathcal{J}$, i.e., the discrepancy between the results obtained by the corrected SA model [Eq. (4)] and those determined in the experiments, subject to the governing equations and the SA model. This is expressed as

$$\begin{aligned} &\text{minimize } \mathcal{J} = \int_{\boldsymbol{x}} \left[\varphi(\beta) - \varphi_{Exp}\right]^2 \mathrm{d}\boldsymbol{x}, \\ &\text{subject to } \mathcal{R}(\beta, \boldsymbol{U}, \tilde{\nu}) = 0, \end{aligned} \tag{5}$$

where φ represents the predicted variables selected as the observation. $\mathcal{R} = (\mathcal{R}_{\mathrm{NS}}, \mathcal{R}_{\mathrm{C}}, \mathcal{R}_{\mathrm{SA}}/\xi_1)$ are the incompressible steady-state N–S equations, the continuity equation, and the model equation presented in Eq. (4), respectively. ξ_1 is a dimension converter of dimensions $[\mathrm{L}^2]$ and value unity to cope with the dimensional inconsistency. We thus obtain a constraint optimization problem solvable by introducing a Lagrange function $\mathcal{L}$

$$\mathcal{L} = \mathcal{J} + \int_{\Omega} (\boldsymbol{V}, q, \tilde{\omega}) \mathcal{R} d\Omega. \tag{6}$$

Here, the adjoint velocity $\boldsymbol{V}$, the adjoint pressure q, and the adjoint turbulence quantities $\tilde{\omega}$ are introduced as the Lagrange multipliers. Ω represents the computational domain. The determination of the optimal β distribution can be achieved by obtaining the sensitivities of the Lagrange function $\mathcal{L}$ with respect to the state variables. Following Othmer,[17] the total variation of $\mathcal{L}$ must be calculated

$$\delta\mathcal{L} = \delta_\beta \mathcal{L} + \delta_{\boldsymbol{U}} \mathcal{L} + \delta_p \mathcal{L} + \delta_{\tilde{\nu}} \mathcal{L}. \tag{7}$$

This can be simplified by choosing the appropriate adjoint variables $\boldsymbol{V}$, q, and $\tilde{\omega}$ to deplete the variation with respect to the state variables

$$\delta_{\boldsymbol{U}} \mathcal{L} + \delta_p \mathcal{L} + \delta_{\tilde{\nu}} \mathcal{L} = 0. \tag{8}$$

Therefore, the sensitivities can be obtained using the variation in $\mathcal{L}$ with respect to β

$$\delta\mathcal{L} = \delta_\beta \mathcal{J} + \int_{\Omega} (\boldsymbol{V}, q, \tilde{\omega}) \delta_\beta \mathcal{R} d\Omega. \tag{9}$$

According to Eq. (8), the adjoint equation associated with the adjoint state variables $\boldsymbol{V}$, q, and $\tilde{\omega}$ can be derived. This reads

$$\begin{aligned} &\delta_{\boldsymbol{U}} \mathcal{J} + \delta_p \mathcal{J} + \delta_{\tilde{\nu}} \mathcal{J} + \int_{\Omega} (\boldsymbol{V}, q, \tilde{\omega}) \delta_{\boldsymbol{U}} \mathcal{R} \mathrm{d}\Omega \\ &\quad + \int_{\Omega} (\boldsymbol{V}, q, \tilde{\omega}) \delta_p \mathcal{R} \mathrm{d}\Omega + \int_{\Omega} (\boldsymbol{V}, q, \tilde{\omega}) \delta_{\tilde{\nu}} \mathcal{R} \mathrm{d}\Omega = 0 \end{aligned} \tag{10}$$

with

$$\delta_{\boldsymbol{U}} \mathcal{R}_{\mathrm{NS}} = \delta U_j \frac{\partial U_i}{\partial x_j} + U_j \frac{\partial \delta U_i}{\partial x_j} - \frac{\partial}{\partial x_j}\left[(\nu + \nu_t)\frac{\partial \delta U_i}{\partial x_j}\right], \tag{11a}$$

$$\delta_{\boldsymbol{U}} \mathcal{R}_{\mathrm{C}} = -\frac{\partial \delta U_j}{\partial x_j}, \tag{11b}$$

$$\delta_{\boldsymbol{U}} \mathcal{R}_{\mathrm{SA}} = \delta U_j \frac{\partial \tilde{\nu}}{\partial x_j}, \tag{11c}$$

$$\delta_p \mathcal{R}_{\mathrm{NS}} = \frac{\partial \delta p}{\partial x_i}, \tag{12a}$$

$$\delta_p \mathcal{R}_{\mathrm{C}} = 0, \tag{12b}$$

$$\delta_p \mathcal{R}_{\mathrm{SA}} = 0, \tag{12c}$$

$$\delta_{\tilde{\nu}} \mathcal{R}_{\mathrm{NS}} = -\frac{\partial}{\partial x_j}\left(f_{\nu 1} \delta\tilde{\nu} \frac{\partial U_i}{\partial x_j}\right), \tag{13a}$$

$$\delta_{\tilde{\nu}} \mathcal{R}_{\mathrm{C}} = 0, \tag{13b}$$

$$\begin{aligned} \delta_{\tilde{\nu}} \mathcal{R}_{\mathrm{SA}} = {} & U_j \frac{\partial \delta\tilde{\nu}}{\partial x_j} - \frac{\partial}{\partial x_j}\left[\frac{\delta\tilde{\nu}}{\sigma_{\nu t}}\frac{\partial \tilde{\nu}}{\partial x_j} + \left(\frac{\tilde{\nu}}{\sigma_{\nu t}} + \frac{\nu}{\sigma_{\nu t}}\right)\frac{\partial \delta\tilde{\nu}}{\partial x_j}\right] \\ & - 2\frac{C_{b2}}{\sigma_{\nu t}}\frac{\partial \delta\tilde{\nu}}{\partial x_j}\frac{\partial \tilde{\nu}}{\partial x_j} - \beta C_{b1}\tilde{S}\delta\tilde{\nu} + 2C_{w1} f_w \frac{\delta\tilde{\nu}}{{d_w}^2}\tilde{\nu}. \end{aligned} \tag{13c}$$

It is noteworthy that $f_{\nu 1}, f_w$, and $\tilde{S}$ are regarded as model coefficients, while their variations with respect to the state variables are neglected for simplification. The deduction of the adjoint system is similar to the description by Othmer;[17] the detailed process is thus not included herein. The adjoint equations and the corresponding boundary conditions are shown as follows. It is noteworthy that the fluid density is absorbed in the primal and adjoint pressures.

Adjoint equations:

$$\begin{aligned} & V_j \frac{\partial U_j}{\partial x_i} - U_j \frac{\partial V_i}{\partial x_j} - \frac{\partial}{\partial x_j}\left[(\nu + \nu_t)\frac{\partial V_i}{\partial x_j}\right] \\ & \quad + \frac{\partial q}{\partial x_i} - \frac{\tilde{\nu}}{\xi_1}\frac{\partial \tilde{\omega}}{\partial x_i} + \frac{\partial \mathcal{J}_\Omega}{\partial \boldsymbol{U}} = 0, \end{aligned} \tag{14a}$$

$$\frac{\partial V_j}{\partial x_j} - \frac{\partial \mathcal{J}_\Omega}{\partial p} = 0, \tag{14b}$$

$$\begin{aligned} & -U_j \frac{\partial \tilde{\omega}}{\partial x_j} - \frac{\partial}{\partial x_j}\left[\left(\frac{\tilde{\nu}}{\sigma_{\nu t}} + \frac{\nu}{\sigma_{\nu t}}\right)\frac{\partial \tilde{\omega}}{\partial x_j}\right] + \frac{1 + 2C_{b2}}{\sigma_{\nu t}}\frac{\partial \tilde{\nu}}{\partial x_j}\frac{\partial \tilde{\omega}}{\partial x_j} \\ & \quad + \left(2\frac{C_{b2}}{\sigma_{\nu t}}\frac{\partial^2 \tilde{\nu}}{\partial {x_j}^2} - \beta C_{b1}\tilde{S} + 2C_{w1} f_w \frac{\tilde{\nu}}{{d_w}^2}\right)\tilde{\omega} \\ & \quad + \xi_1 f_{\nu 1}\frac{\partial V_i}{\partial x_j}\frac{\partial U_i}{\partial x_j} - \xi_1 \frac{\partial \mathcal{J}_\Omega}{\partial \tilde{\nu}} = 0. \end{aligned} \tag{14c}$$

Adjoint boundary conditions:

For the inflow, the wall and far-field boundaries where the primal state variables $\boldsymbol{U}$ and $\tilde{\nu}$ are specified as follows,

$$\boldsymbol{V}_\tau = 0, \quad \boldsymbol{V}_n = -\frac{\partial \mathcal{J}_\Gamma}{\partial p}, \tag{15a}$$

$$\frac{\partial q}{\partial x_i} \cdot \boldsymbol{n} = 0, \tag{15b}$$

$$\tilde{\omega} = 0. \tag{15c}$$

On the outflow boundaries where the wall-normal gradients of the primal state variables $\boldsymbol{U}$ and $\tilde{\nu}$ are zero,

$$\boldsymbol{U}_n \cdot \boldsymbol{V}_\tau + (\nu + \nu_t)\left(\frac{\partial \boldsymbol{U}_\tau}{\partial x_i} \cdot \boldsymbol{n}\right) + \frac{\partial \mathcal{J}_\Gamma}{\partial \boldsymbol{U}_\tau} = 0, \tag{16a}$$

$$\boldsymbol{U}_n \cdot \boldsymbol{V}_n + (\nu + \nu_t)\left(\frac{\partial \boldsymbol{U}_n}{\partial x_i} \cdot \boldsymbol{n}\right) + \frac{\tilde{\nu}\tilde{\omega}}{\xi_1} + \frac{\partial \mathcal{J}_\Gamma}{\partial \boldsymbol{U}_n} - q = 0, \tag{16b}$$

$$\begin{aligned} & \boldsymbol{U}_n \tilde{\omega} + \left(\frac{\tilde{\nu}}{\sigma_{\nu t}} + \frac{\nu}{\sigma_{\nu t}}\right)\left(\frac{\partial \tilde{\omega}}{\partial x_i} \cdot \boldsymbol{n}\right) \\ & \quad - \xi_1 f_{\nu 1}\left(V_i \frac{\partial U_i}{\partial x_j} \cdot \boldsymbol{n}\right) + \xi_1 \frac{\partial \mathcal{J}_\Gamma}{\partial \tilde{\nu}} = 0, \end{aligned} \tag{16c}$$

with

$$\mathcal{J} = \int_{\Gamma} \mathcal{J}_{\Gamma} \mathrm{d}\Gamma + \int_{\Omega} \mathcal{J}_{\Omega} \mathrm{d}\Omega, \tag{17}$$

where Γ represents the boundary of the computational domain.

Equations (15) and (16) provide the boundary conditions for $\boldsymbol{V}$, q, and $\tilde{\omega}$. It is noteworthy that Eq. (16a) only specifies the tangential component of the adjoint velocity $\boldsymbol{V}_{\tau}$ on the outflow boundary. A straightforward treatment for the normal component $\boldsymbol{V}_n$ is the zero-gradient condition. However, Eq. (16a) provides a tangential component condition that is highly sensitive to the primal velocity; this induces the serious instability for the adjoint equations. Fortunately, this outflow boundary condition contributes little to the adjoint flow field inside the domain, while the adjoint flow field largely originates from the source term $\frac{\partial \mathcal{J}_{\Omega}}{\partial \boldsymbol{U}}$ in Eq. (14a) and the boundary condition on the wall [Eq. (15a)], and propagates upstream in a direction opposite to the primal flow. The zero-tangential component of the adjoint velocity is a good choice to significantly improve the numerical stability without deterioration on the results. The second source of the numerical instability in the computation is the adjoint transpose convection (ATC) term

$$\mathrm{ATC}_i = V_j \frac{\partial U_j}{\partial x_i}. \tag{18}$$

Here, the formulation is different from that derived by Othmer.[17] Schramm *et al.*[23] reported that integration by parts is unnecessary in the derivation of the ATC term; this leads to the current more stable adjoint momentum equation. Georgios *et al.*[24] damped the ATC contribution on a cell-by-cell basis in the regions where the projected diagonal contribution for an implicit ATC term is negative, and claimed that this guaranteed the diagonal dominance of the matrix, and rendered the solution more stable. However, this criterion is not universal and is conservative in certain cases as much of the ATC contribution is damped. In the present study, the instability is eliminated by the additional numerical dissipation introduced by the first-order upwind scheme applied for the convection term of the adjoint momentum equations, while the primal equations still retain the second-order accuracy. Figure 2 shows that the first-order scheme has little effect on the accuracy of the final result, compared to the second-order scheme. The third source of the numerical instability is the third term in Eq. (14c), where the explicit gradient of $\tilde{\omega}$ is involved (it must be treated explicitly when coded in OpenFOAM). In the present study, the gradient of $\tilde{\omega}$ is reconstructed from its surface flux, serving as the computation on a pseudo staggered grid. This helps removing the "wiggle behaviors" and improving the numerical stability.

C. Specialization to wall-pressure assimilation

Using the pressure coefficient on the wall as the observation data, the cost function $\mathcal{J}$ is presented as

$$\mathcal{J} = \xi_2 \int_{\Gamma_w} \left(\frac{p - p_{\mathrm{Exp}}}{0.5 U_{\infty}^2} \right)^2 \mathrm{d}\Gamma_w + \alpha \phi \frac{\xi_2}{\sqrt{\xi_1}} \int_{\Omega} (\beta - 1)^2 d\Omega. \tag{19}$$

Here, p_{Exp} is the measured pressure on the wall boundary. ξ_2 is a dimension converter of dimensions $[\mathrm{L}^3 \cdot \mathrm{T}^{-3}]$ and value unity to ensure dimensional consistency. U_{∞} denotes the free-stream velocity. α is the dimensionless weighting coefficient specifying the relative importance of the second term in the cost function. ϕ is the blending function defined as

$$\phi = 0.5 \left(1 - \frac{\beta - 1}{|\beta - 1| + \varepsilon} \right), \tag{20}$$

with a small positive constant ϵ to prevent the denominator from zero. In this formulation, ϕ becomes unity in the region where $\beta < 1$, while the second term in Eq. (19) is activated. With this mechanism, the solution is pushed toward a large β value such that the steadiness of the primal flow is guaranteed. Therefore, the sources in the adjoint equations and boundary conditions become

$$\frac{\partial \mathcal{J}_{\Omega}}{\partial \boldsymbol{U}} = 0, \tag{20a}$$

$$\frac{\partial \mathcal{J}_{\Omega}}{\partial p} = 0, \tag{20b}$$

$$\frac{\partial \mathcal{J}_{\Omega}}{\partial \tilde{\nu}} = 0, \tag{20c}$$

$$\frac{\partial \mathcal{J}_{\Gamma}}{\partial \boldsymbol{U}_{\tau}} = 0, \quad \frac{\partial \mathcal{J}_{\Gamma}}{\partial \boldsymbol{U}_n} = 0, \tag{20d}$$

$$\frac{\partial \mathcal{J}_{\Gamma}}{\partial p} = 8 \cdot \xi_2 \frac{p_{\mathrm{Exp}} - p}{U_{\infty}^4}, \tag{20e}$$

$$\frac{\partial \mathcal{J}_{\Gamma}}{\partial \tilde{\nu}} = 0. \tag{20f}$$

In the adjoint system, the adjoint flow originated from the normal adjoint velocity on the wall boundary, while the adjoint turbulent quantities $\tilde{\omega}$ are produced by the source term [the fourth term in Eq. (14c)]. Both fields are convected upstream by the adjoint system.

D. Specialization to velocity assimilation

In experiments, the flow velocity is typically obtained on straight lines such as using a hot-wire anemometer and laser Doppler velocimetry (LDV), or in limited two-dimensional (2D) planes such as using planar particle image velocimetry (planar-PIV) inside the flow domain. In addition, the measured velocity is typically limited to one or two components. In the present study, the streamwise component of the velocity U_x on several straight lines inside the domain is used as the observation data; the cost function $\mathcal{J}$ can be subsequently presented as

$$\mathcal{J} = \frac{\xi_2}{\sqrt{\xi_1}} \int_{\Omega} M \left(\frac{U_x - U_{x,\mathrm{Exp}}}{U_{\infty}} \right)^2 \mathrm{d}\Omega + \alpha \phi \frac{\xi_2}{\sqrt{\xi_1}} \int_{\Omega} (\beta - 1)^2 \mathrm{d}\Omega. \tag{21}$$

Here, a masking function M is defined to specify the region where the observation data are obtained. The values of M at the cell centers close to the lines are set to unity and remain zero in other regions. Therefore, the sources in the adjoint equation and boundary conditions become

$$\frac{\partial \mathcal{J}_{\Omega}}{\partial \boldsymbol{U}} = 2M \frac{\xi_2}{\sqrt{\xi_1}} \frac{\boldsymbol{U} - \boldsymbol{U}_{\mathrm{Exp}}}{U_{\infty}^2}, \tag{22a}$$

$$\frac{\partial \mathcal{J}_{\Omega}}{\partial p} = 0, \tag{22b}$$

$$\frac{\partial \mathcal{J}_{\Omega}}{\partial \tilde{\nu}} = 0, \tag{22c}$$

$$\frac{\partial \mathcal{J}_\Gamma}{\partial \boldsymbol{U}_\tau} = 0, \quad \frac{\partial \mathcal{J}_\Gamma}{\partial \boldsymbol{U}_n} = 0, \tag{22d}$$

$$\frac{\partial \mathcal{J}_\Gamma}{\partial p} = 0, \tag{22e}$$

$$\frac{\partial \mathcal{J}_\Gamma}{\partial \tilde{\nu}} = 0, \tag{22f}$$

with the assignment

$$U_{y,\mathrm{Exp}} = MU_y, \tag{23a}$$

$$U_{z,\mathrm{Exp}} = MU_z, \tag{23b}$$

at each iteration to ensure that only the streamwise component of the velocity is assimilated. In this case, both the adjoint flow and the turbulent quantities $\tilde{\omega}$ originated from the internal source.

E. Correcting function determination

Once the adjoint state variables are obtained, the sensitivities of the Lagrange function $\mathcal{L}$ with respect to the correcting function β can be computed from Eq. (9) for both the cases of wall-pressure and velocity assimilations

$$\frac{\partial \mathcal{L}}{\partial \beta} = 2\alpha\phi\frac{\xi_2}{\sqrt{\xi_1}}(\beta - 1) - \frac{C_{b1}\tilde{S}\tilde{\nu}\tilde{\omega}}{\xi_1}. \tag{24}$$

As the sensitivity with respect to the state variables is forced to vanish [Eq. (8)], the correction function β can be adjusted gradually according to Eq. (24) to minimize the cost function. This is achieved using the steepest descent algorithm[25] at each iteration

$$\beta = \beta - \lambda\frac{\partial \mathcal{L}}{\partial \beta}, \tag{25}$$

with λ being the step length that can be estimated using

$$\lambda = (0.01 \sim 0.1)/\left(\frac{\partial \mathcal{L}}{\partial \beta}\right)_{\max}. \tag{26}$$

This indicates that β has an adjustment of 0.01–0.1 at each iteration. The numerical instability benefits from a smaller value of λ at the expense of the convergence speed. As the primal and adjoint equations, and the adjustment of β are coupled at each iteration in the present study, a small value of λ is required for the accurate determination of the sensitivity. Therefore, the optimization of the step length is not implemented presently. β converges to the optimal distribution as the residual, i.e., the difference between the predicted and observed data, or the maximum value of the sensitivity, decreases below a specified value.

III. TEST CASES

A. Flow over a cylinder

The flow over a two-dimensional cylinder is employed in this study to demonstrate the effects of different discretization schemes applied to the adjoint momentum equations on the assimilation results. The Reynolds number based on the cylinder diameter D is $Re = 20\,000$. A two-dimensional domain extended $5D$, $16D$, and $30D$ in the upstream, lateral, and downstream directions, respectively, is employed with 50 000 grid cells which achieve the grid independence. Free-slip and zero-gradient conditions are applied on the lateral and outflow boundaries, respectively, while all the boundary conditions for the adjoint variables are set according to the discussion in Sec. II. The default SA simulation is performed with $\tilde{\nu} = 0.001$ on the inflow boundary. Subsequently, another simulation with the SA mode is conducted with an inflow boundary condition $\tilde{\nu} = 0.01$ to produce the reference data (synthetic observation); this produces a recirculation bubble in the cylinder wake that is much shorter than that in the former simulation with $\tilde{\nu} = 0.001$. The objective of the ABDA model used in this case is to reproduce the flow field in the reference configuration using the inflow condition $\tilde{\nu} = 0.001$. Using the reference synthetic data as the observation makes the convergence easier to compare the effects of different discretize schemes. The observation data are extracted at $2D$ downstream of the cylinder from the reference data. The convection terms in all the primal equations are discretized using a linear-upwind scheme, which is derived from the upwind scheme and returns the upwind weighting factors and applies an explicit correction to achieve the boundedness and second-order accuracy (named second-order scheme for simplification), while both the second-order scheme and first-order upwind are used for the adjoint momentum equations for comparison. α is set to 1×10^{-6} to eliminate any constraint on the β determination.

Figures 1(a) and 1(b) present the distributions of the initial adjoint state variables (the velocity magnitude and turbulence quantities) calculated using different discretization schemes before the update of β. The difference in the adjoint state variable distributions is expectably small. The adjoint velocities remain significantly large near the cylinder and produce two abreast recirculation bubbles in the wake; the adjoint velocities are convected upstream in the far-cylinder region. Additionally, large $\tilde{\omega}$ values are observed in the cylinder shear layer. It is noteworthy that negative values of $\tilde{\omega}$ are produced, unlike the primal counterpart $\tilde{\nu}$ that is always positive. In addition, both the adjoint variables decrease to extremely small (not shown here) as the computation converges, and the difference between the simulation result and the observation (i.e., origin of the source in the adjoint equations) is eliminated. Figure 1(c) presents the converged β distributions calculated using different discretization schemes that are the optimal β distributions for the flow reproduction. A significant difference in the β distributions is observed using the first- and second-order schemes, even though the initial adjoint variables are similar. This is because the adjoint method drives the cost function to the local minima; thus, the resulting solution is not unique.[26] It is also noteworthy that because the observation data are obtained by imposing different $\tilde{\nu}$ on the inflow boundary, different eddy viscosity distributions will be resulted in the entire domain. The present results indicate that the approximation of the flow field using the ABDA model is possible without the complete recovery of the eddy viscosity distribution.

The quantitative comparison of the assimilation results using different discretization schemes are presented in Fig. 2. While the default SA simulation yields a result that deviates significantly from the reference experimental data, good agreement on the assimilated velocity and pressure coefficient

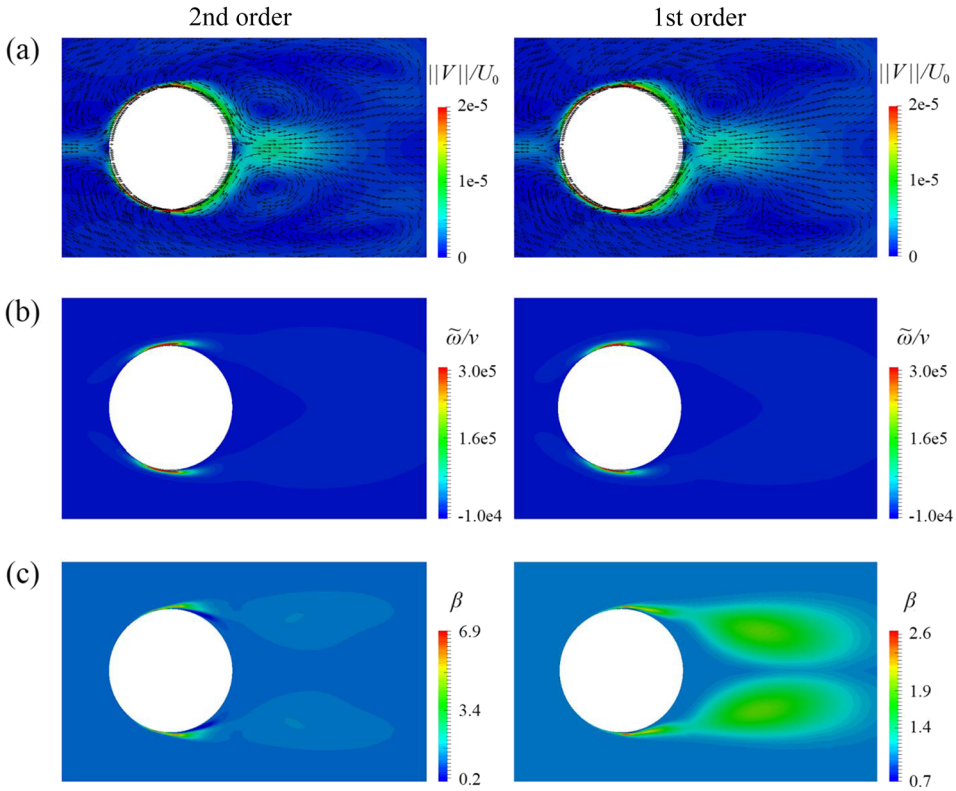

FIG. 1. Distributions of the adjoint variables ν (a), $\tilde{\omega}$ (b), and the correction coefficient β (c) in the cylinder wake.

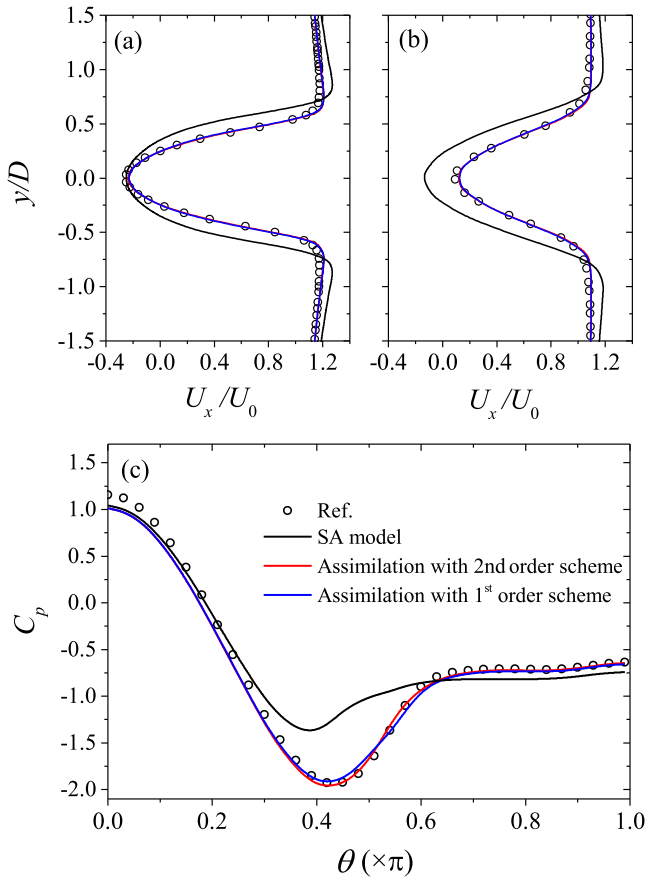

FIG. 2. Streamwise velocity [(a) $x/D = 1$ and (b) $x/D = 2$] and pressure coefficient [(c) on the cylinder] distributions calculated using the SA model and ABDA model with the U_x constraint. (The reference observational data here are produced using the default SA simulation with different inflow boundary conditions.)

with the reference data is obtained using both first- and second-order schemes. This indicates that both the β distributions shown in Fig. 1(c) are well suited for the flow field reproduction, even though they differ significantly from each other. It is important to note here that the optimal β distributions change the entire balance of the turbulence in the flow and thus improve the model prediction. The multi-optimal problem may stem from the eddy viscosity hypothesis of the RANS model, which reduces the Reynolds stress tensor to an eddy viscosity scalar. The time-lasting effects of the production mechanism observed by Meldi[27] is not considered recently as the present formulation is proposed only for steady simulations. Figure 2 also demonstrates that the first-order discretization schemes applied on the adjoint equations do not deteriorate the assimilation results much, when the primal equations are solved precisely. Therefore, the first-order upwind scheme is applied on the adjoint equations for all the following cases for numerical stability, while the second-order scheme is retained for the primal equation.

B. Free round jet

The free round jet is an important flow configuration to evaluate the model in the shear flow. It is well known that RANS models cannot capture the basic flow features in round jets, thus exhibiting poor performance in predicting the mean flow field.[28] The free jet issued from a long pipe at the Reynolds number based on the pipe diameter D and bulk velocity U_0, i.e., Re = 6,000, which has been studied experimentally and numerically in our previous research,[19] is employed. A quasi two-dimensional computational domain with maximum diameter $28D$ and length $32D$ (50 000 grid cells after the grid independent test) is used for the present ABDA model. The

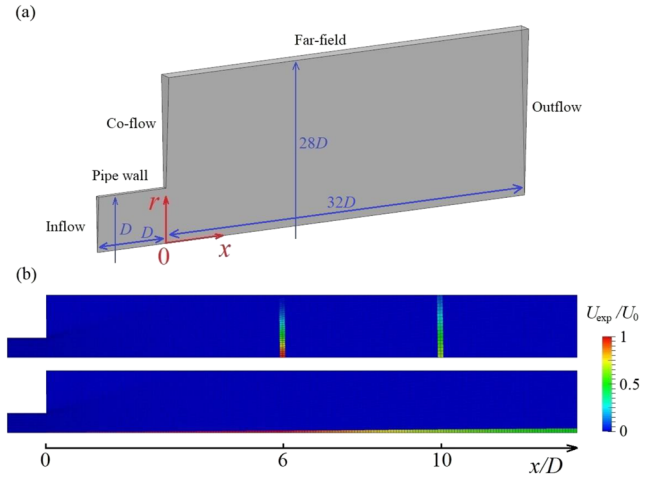

FIG. 3. Computational domain of the free jet (a) and the implantation of the experimental data (b).

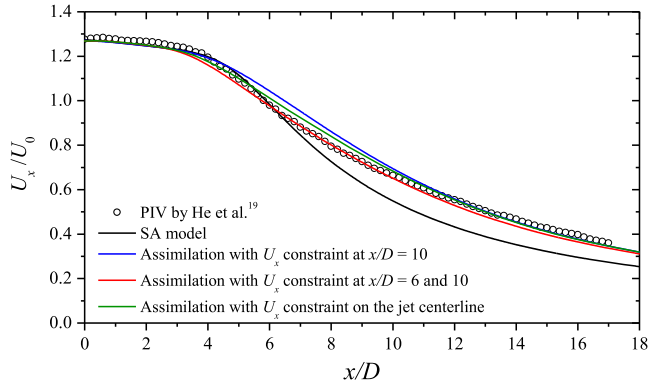

FIG. 4. Streamwise velocity on the jet centerline calculated using the SA and ABDA models.

inflow boundary is extended $1D$ upstream of the nozzle exit to eliminate the boundary effect on the results, as shown in Fig. 3(a). A precursor simulation is conducted to obtain the inflow boundary condition for the primal state variables. A co-flow with 2% of the jet bulk velocity is imposed to improve the numerical stability. The free-slip and zero-gradient conditions are imposed on the far-field and outflow boundary, respectively, for the primal state variables. All the boundary conditions for the adjoint variables are set according to the discussion in Sec. II. Figure 3(b) shows various implantations of the PIV data in the assimilation: the first constraint is using the observation at $x/D = 6$, while the second constraint is using the observations at $x/D = 6$ and 10, to improve the performance. Two nearest columns of the grid cell at both sides of the specified radial line ($x/D = 6$ or 10) are selected, on which the value of the M equals unity and $U_{x,\mathrm{Exp}}$ equals the corresponding PIV data. The third constraint uses the PIV data on the jet centerline, while the nearest cells are selected to set the masking function and observation. α is set to 1×10^{-6} to eliminate any constraint on the β determination. Note here that the observation is set on the cell center of the grid; this will indeed induce error while the cell centers are not exactly on the jet centerline.

Figure 4 shows the streamwise velocity along the jet centerline determined by PIV, the default SA model, and the ABDA model with different observations. It is obvious that the result predicted using the SA model deviates significantly from the PIV data at $x/D > 6$. The best agreement is obtained using the ABDA model with the observations at $x/D = 6$ and 10. The assimilation results with other observations also exhibit significant improvements compared with that of the default SA model. However, using the observation at only $x/D = 10$ shows an insufficient constraint in the

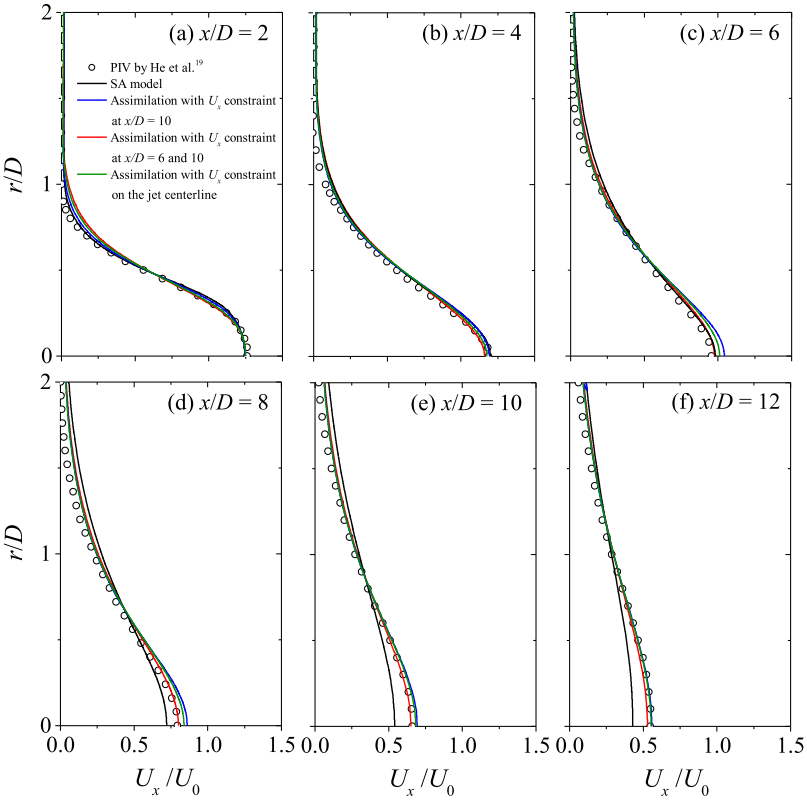

FIG. 5. Transverse profiles of the streamwise velocity in the free jet calculated using the SA and ABDA models.

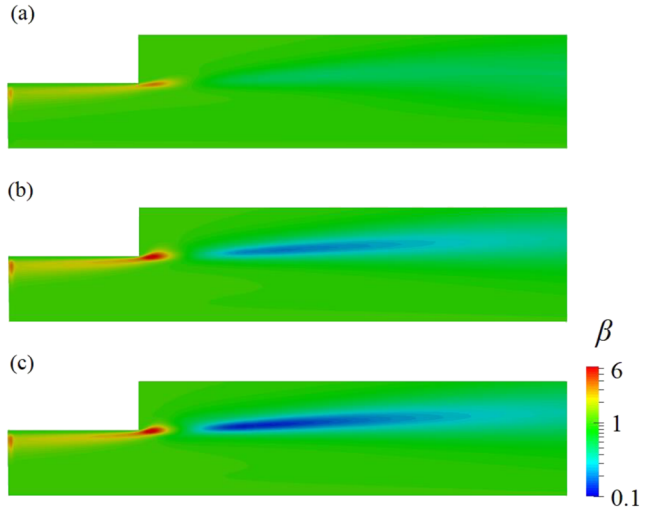

FIG. 6. Correction coefficient β distributions in the free jet calculated using different U_x constraints. (a) U_x constraints at $x/D = 10$. (b) U_x constraints at $x/D = 6$ and 10. (c) U_x constraints on the jet centerline.

region $6 < x/D < 10$, where the streamwise velocity is slightly overpredicted. This indicates that an appropriate selection of the observations is necessary to impose a sufficient constraint on the assimilated field. In the present jet, the observation at $x/D = 6$ is a good constraint to accurately capture the feature of the jet transition downstream of the potential core, and the observation at $x/D = 10$ is required for the prediction of the velocity decay beyond the transition region. A detailed quantitative comparison of the streamwise velocity in the cross sections is presented in Fig. 5, showing the excessive spread and decay of the jet predicted using the SA model as well as the accurate reproduction of the global field using the ABDA model.

Figure 6 shows the distributions of the correcting function β computed with different observations. The distribution patterns are similar except the absolute values. A significantly large value of β is observed near the wall boundary and the nozzle tip, while a small value is produced in the jet shear layer. Obviously, the small value of β is responsible for the decrease in the turbulence eddy viscosity, as shown in Fig. 7, and thus the jet decay rate beyond the jet potential core. It is noteworthy that a region with a large β exists close to the inflow boundary (Fig. 6) owing to the boundary condition of the adjoint variables. However, this region has little effect on the eddy viscosity distribution (Fig. 7) owing to the low shear rate of the flow.

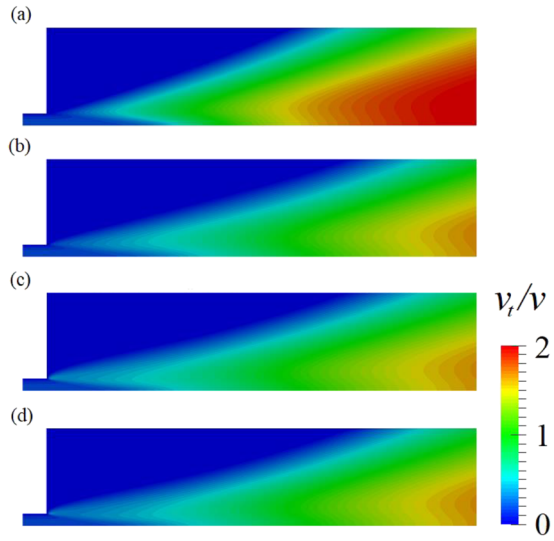

FIG. 7. Turbulence eddy viscosity distributions in the free jet calculated using (a) the SA model and the ABDA model with different U_x constraints. (b) Assimilation with U_x constraints at $x/D = 10$. (c) Assimilation with U_x constraints at $x/D = 6$ and 10. (d) Assimilation with U_x constraints on the jet centerline.

C. Flow over a hump

The two-dimensional flow over a wall-mounted hump (without flow control) with the available original data[20,21] is employed in this study to test the ABDA model, in the prediction of flow separation from a smooth surface, and the subsequent reattachment and boundary recovery. This particular case has proven to be challenging for all known RANS models (*NASA Turbulence Modeling Resource*, https://turbmodels.larc.nasa.gov/), which tend to underpredict the turbulent shear stress in the separated shear layer and therefore tend to predict too long a separation bubble. The Reynolds number based on the freestream velocity U_0 and the hump chord C is 936 000. The inflow boundary condition is imposed at $x/C = -2.14$ with a boundary layer thickness of $0.08C$ and a velocity profile obtained by a precursor SA simulation. The computational domain is presented in Fig. 8(a), where the location of the far-field boundary (free-slip) is determined $0.7C$ from the bottom wall to fit the blockage in the experiment; this treatment is also applied in *NASA Turbulence Modeling Resource* and in the study by Krishnan *et al.*[29] to reduce the domain size with respect to the measurement configuration. A precursor SA simulation is conducted to obtain the desired boundary layer thickness on the inflow boundary, while the walls and outflow boundaries are set as no-slip and zero-gradient conditions, respectively. All the boundary conditions for the adjoint variables are set according to the discussion in Sec. II. A set of two-dimensional grids with

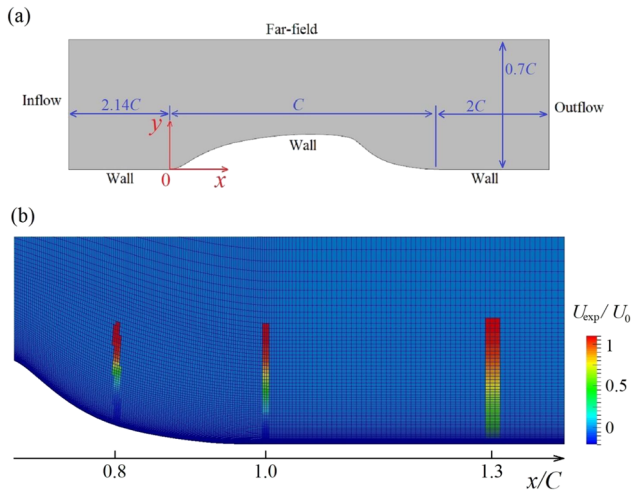

FIG. 8. Computational domain of the hump flow (a) and the implantation of the experimental data (b).

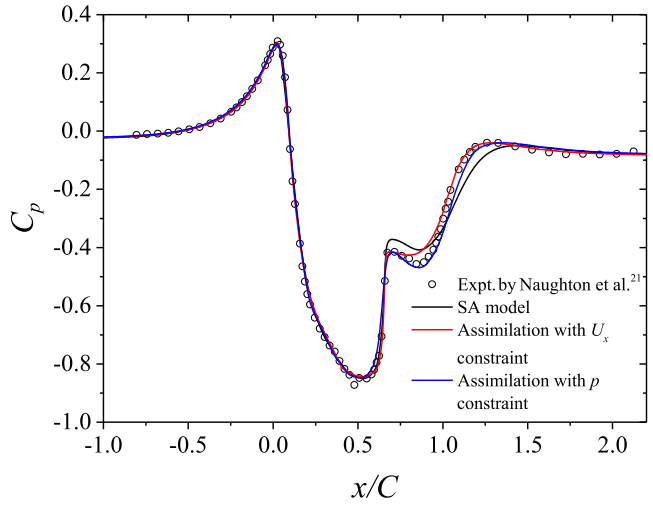

FIG. 9. Pressure coefficients on the hump calculated using the SA and ABDA models.

0.1×10^6 cells (after the grid independent test) is generated as shown in Fig. 8(b), with the experimental data (streamwise component of the velocity) implanted at $x/C = 0.8$, 1.0, and 1.3 as the observations (U_x constraint). It is noteworthy that three columns of the grid cell at each implantation location are assigned with the experimental data to demonstrate that a slight extension of the experimental data to the nearby cells will not influence the assimilation result significantly. Additionally, the pressure coefficient on the surface at $0 < x/C < 1.5$ (p constraint) is employed as another observation to test the performance of the ABDA model for the flow field reproduction. In the present case, the α value is also set to 1×10^{-6} to eliminate any constraint on the β determination.

The pressure coefficient on the surface predicted by the SA model and the ABDA model with U_x and p constraints is presented in Fig. 9. The SA model yields a pressure coefficient exhibiting a significant disagreement with the experimental data in the region $0.7 < x/C < 1.3$, owing to its problematic behavior in the flow separation. The prediction is significantly improved using the ABDA model with both constraints. However, a slight deviation is still observed near $x/C = 0.8$, resulting from the error in the flow field production [Fig. 10(c)]. It is noteworthy that the agreement of the pressure coefficient with the experimental data is less impressive as that determined using the discretized adjoint method;[12] this is attributed to the uncertainty in the sensitivity computation owing to several mathematical simplifications in the ABDA formulation and the first-order scheme employed in the adjoint equations.

The streamwise velocity in the flow separation and reattachment region reproduced by the SA and ABDA models is presented in Fig. 10. We observed that the velocity is significantly underestimated at $x/C > 1.0$, indicating too long a recirculation bubble determined by the SA model; this agrees with the SA simulation results shown in the *NASA Turbulence Modeling Resource* database. The ABDA model with the U_x constraint reproduces the recirculation bubble accurately while maintaining the flow field in the separation region nearly unaffected. The result obtained using the ABDA model with the p constraint still exhibited a large gap compared with the experimental data in the region of boundary recovery. This suggests that the velocity inside the domain is better for the assimilation observation. However, it is noteworthy that both the SA and ABDA models failed to reproduce the near-wall flow at $x/C = 0.8$ [Fig. 10(c)] even though the velocity there has been constrained to the experimental data. This is likely from the defect of the eddy-viscosity hypothesis used in the RANS model; this also gives rise to the local disagreement of the pressure coefficient with the experimental data as mentioned before.

Figure 11 presents the distinctly different β distributions computed using the ABDA model using different observations. This evidences the multisolution property of the adjoint method that drives the result to the nearest local minima. It

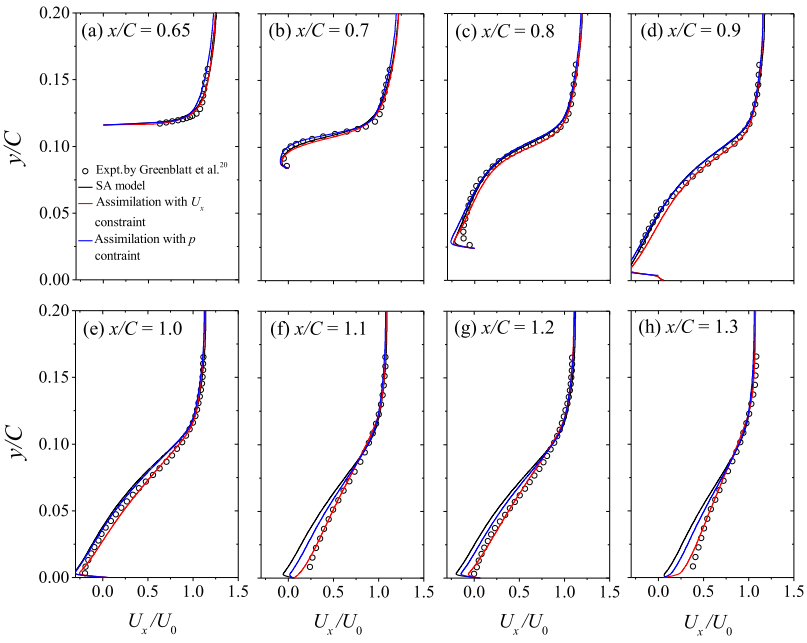

FIG. 10. Streamwise velocity profiles in hump flow calculated using the SA and ABDA models.

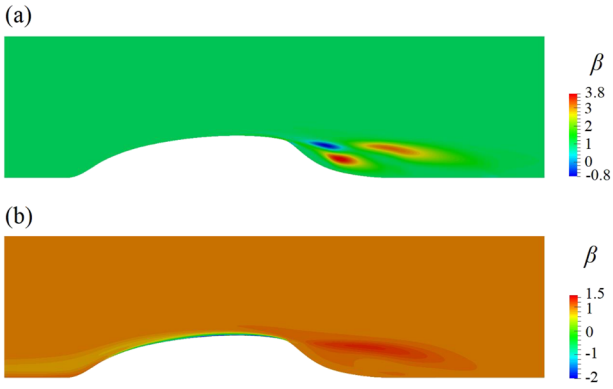

FIG. 11. Correction coefficient β distributions in hump flow calculated using (a) U_x and (b) pressure (p) constraints.

is noteworthy that the negative value of β is observed in both cases, indicating the turbulence damping and thus the reduction in the eddy viscosity. The correction of the SA model using the U_x constraint primarily occurs in the separated shear layer, as shown in Fig. 11(a); this is reasonable as it is where the observation data are extracted and where the flow is highly sensitive. Alternatively, the correction using the p constraint exists largely near the hump wall with the strongest turbulence damping, as shown in Fig. 11(b). This tends to delay the flow separation and decrease the length of the recirculation bubble. However, this effort is hardly sufficient to correct the flow in the reparation region even though the pressure coefficient on the hump is accurately predicted, as shown in Figs. 9 and 10. In addition, too small a β value deteriorates the robustness of the adjoint equations, giving rise to the requirement of a smaller step size λ in the steepest descent algorithm and thus a longer convergence time. The eddy viscosity distributions predicted by the SA and ABDA models are presented in Fig. 12. As shown, the ABDA model with the U_x constraint yields a significant modification on the eddy viscosity in the reparation region, while the ABDA model with the p constraint has very limited effects. This indicates that the U_x constraint strategy is more efficient for the flow field reproduction using the ABDA model.

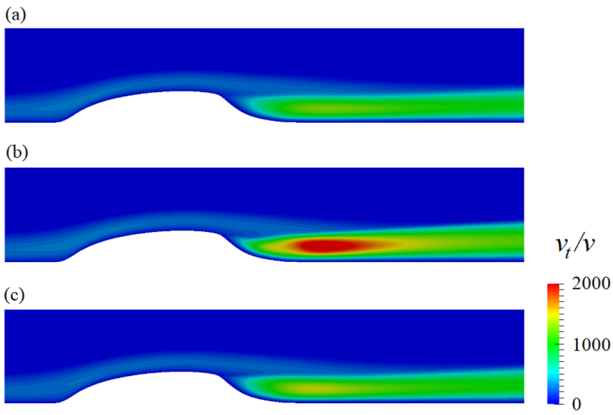

FIG. 12. Turbulence eddy viscosity distributions in hump flow calculated using (a) the SA model and the ABDA model with (b) U_x and (c) pressure (p) constraints.

D. Three-dimensional flow over a wall-mounted cube

The flow over a wall-mounted cube in a confined channel[22] at $Re = 10^5$ is employed to demonstrate the capability of the present ABDA model in three-dimensional flows. This flow is featured by multiple separations and reattachments of the flow and shear-layer interactions, which are challenging for RANS simulations. The full set of experimental data can be found in the *Journal of Fluid Engineering Databank* (https://scholar.lib.vt.edu/ejournals/JFE/data/JFE/). The computational domain employed in this study is presented in Fig. 13(a). A cube of size D is mounted in a $2D$-high channel. The channel width is set to $16D$ to eliminate the lateral confinement to the flow. A precursor SA simulation in a fully developed channel flow is conducted to obtain the inflow boundary condition for the primal variables. The cube surface, and the upper and lower walls are set as the no-slip wall, while free-slip and zero-gradient conditions are applied to the lateral far-field to mimic the experimental condition. All the boundary conditions for the adjoint variables are set according to the discussion in Sec. II. A structured grid with 1×10^6 cells (after the grid independent test, larger number of cells are also solvable using this ABDA model) is employed for demonstration purposes, which is extremely memory consuming or even problematic when used with the discretized adjoint method. Figure 13(b) presents the implantation strategy of the experimental data, with the streamwise component of the velocity at $x/D = 1, 2, 4$ in the center plane, and $x/D = 1, 1.5$ at $z/D = \pm 0.5$ set to the single column of cells as the observations. In the assimilation, α [Eq. (21)] is set to 3×10^{-4} to drive the solution toward a larger β value to eliminate the flow unsteadiness. The selection of α is challenging as a small α value will induce the flow unsteadiness and cause convergence problem (unlike the robustness problem mentioned in Sec. III C) for the adjoint equations, while a large α value drives β toward unity and thus reduces the correction effect to the

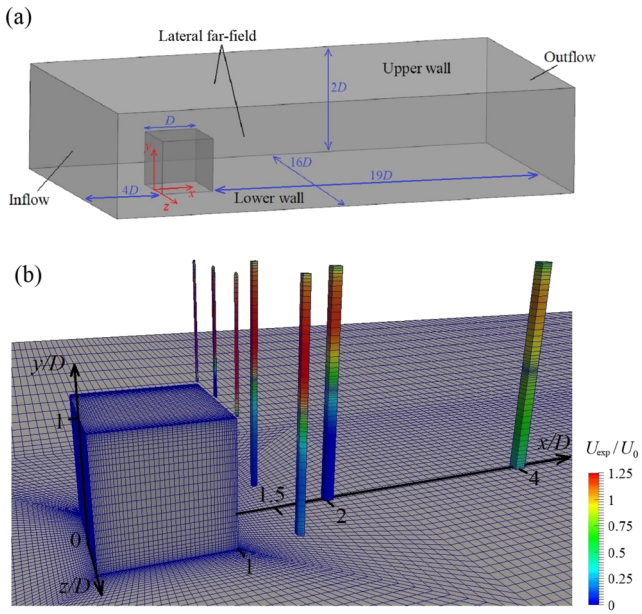

FIG. 13. Computational domain of the 3D cube flow (a) and the implantation of the experimental data (b).

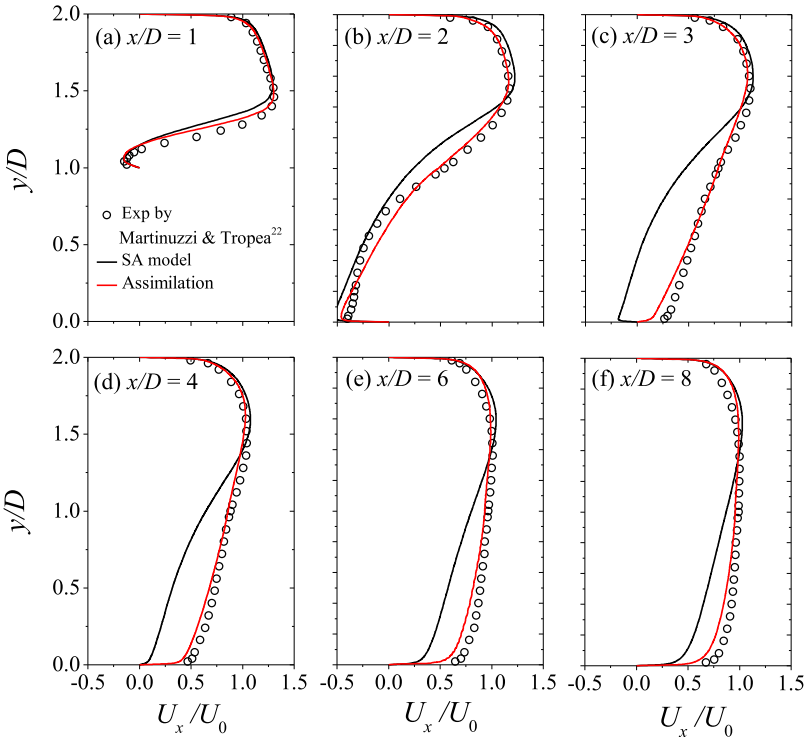

FIG. 14. Streamwise velocity profiles at $z/D = 0$ in 3D cube flow calculated using the SA and ABDA models.

turbulence production. α can be estimated by comparing the first and second terms in Eq. (21) and is decreased gradually in the computation before the flow unsteadiness occurs. It is noteworthy that the constraint of the small β value by increasing α has two different impacts on the final result, which cannot be controlled explicitly. The first impact is forcing β to increase at the expense of the result accuracy, while the second impact is driving β to another solution that will minimize the cost function and provide satisfactory results.

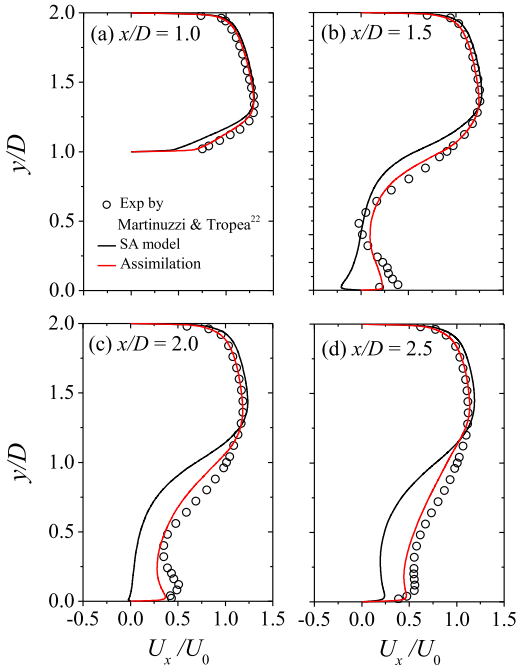

FIG. 15. Streamwise velocity profiles at $z/D = 0.5$ in 3D cube flow calculated using the SA and ABDA models.

Figure 14 shows the profiles of the streamwise velocity on the center plane. The SA model also yields a result with too long a recirculation bubble while the streamwise velocities at $3 \le x/D \le 8$ are severely underestimated. The ABDA model has largely amended this discrepancy while the predicted streamwise velocities agree reasonably well with the experimental data. Figure 15 shows the significant improvement in the velocity prediction on the plane $z/D = 0.5$ at several streamwise locations. On this plane, the ABDA results exhibit a slight discrepancy at $x/D = 1.5$, 2.0, and 2.5 compared with the experimental data. Although the velocity is constrained to the experimental data at $x/D = 1.5$ on this plane, the ABDA reproduction of the flow is less impressive than is expected. This may be attributed to the error in the sensitivity determination, or the β constraint owing to a large α value. Nevertheless, the improvement with respect to the default SA model is significant.

The isosurfaces of the converged β are presented in Fig. 16, with the dark gray representing $\beta = 0.5$ and the

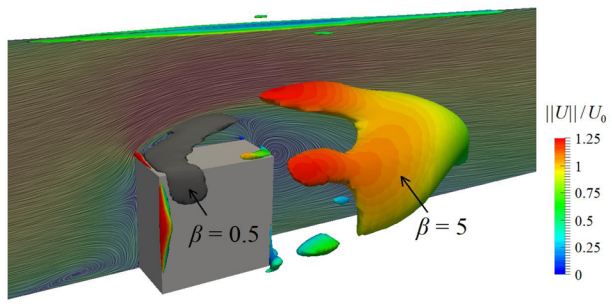

FIG. 16. Isosurface of the correction coefficient $\beta = 0.5$ (colored by dark gray) and $\beta = 5$ (colored by the velocity magnitude) in 3D cube flow calculated with $\alpha = 3 \times 10^{-4}$.

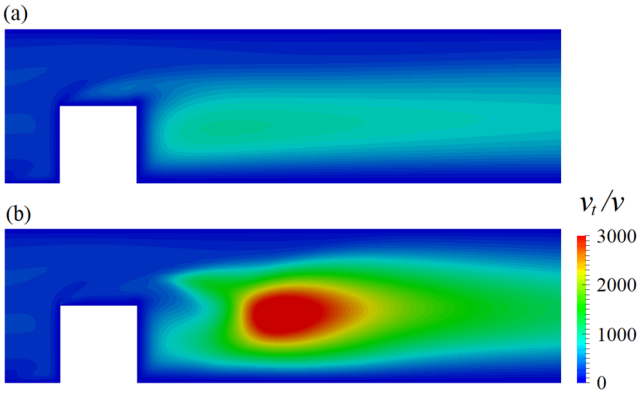

FIG. 17. Turbulence eddy viscosity distributions at $z/D = 0$ in 3D cube flow calculated using (a) the SA model and (b) the ABDA model with $\alpha = 3 \times 10^{-4}$.

velocity-colored surface representing $\beta = 5$. This shows that the ABDA model yields a low value of β above the cube, thus decreasing the eddy viscosity and inducing the flow unsteadiness. Owing to the constraint using a large α value, β remains at this safe value above the cube while the flow is steadily maintained, giving rise to the successful assimilation. The resultant eddy viscosity is presented in Fig. 17. It is shown that using the ABDA model, the eddy viscosity downstream of the cube increased substantially. Meanwhile, a significant attenuation of the eddy viscosity exists above the cube owing to the low value of β.

Figure 18 shows the β distribution and the flow field on the center plane using $\alpha = 1 \times 10^{-6}$, which imposes a little constraint on the β determination. In this case, a large scale of β distributed above the cube is lower than 0.5. This results in the excessive attenuation of the eddy viscosity and induces strong oscillations of the flow in the first separation region above the cube. This oscillation (unable to converge) gives rise to the unsteadiness in the second separation region behind the cube and drives the solution toward an undesired direction far from convergence.

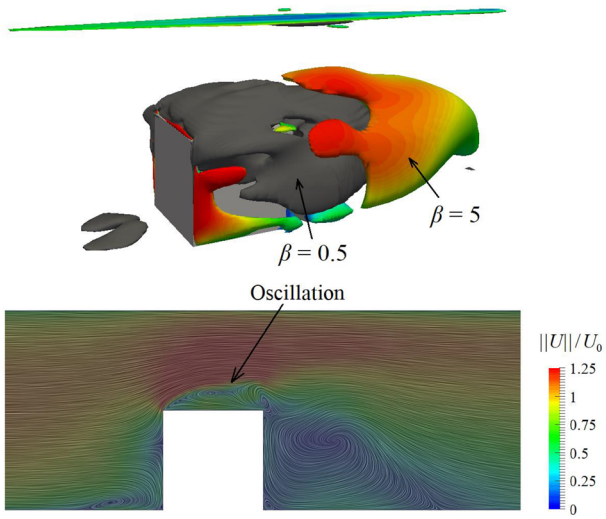

FIG. 18. Isosurface of the correction coefficient $\beta = 0.5$ (colored by dark gray) and $\beta = 5$ (colored by the velocity magnitude) and the streamlines in 3D cube flow calculated with $\alpha = 1 \times 10^{-6}$ (not converged).

IV. CONCLUDING REMARKS

The present study proposed a generalized data assimilation model (the ABDA model) for turbulent flows based on the continuous adjoint formulation. The SA turbulence model was modified by adding a correction function β as a spatially varying coefficient to the turbulence production term. A full set of adjoint equations and the corresponding boundary conditions were derived, coupled with the primal N–S equations and the SA model. The model-form error was thus corrected by optimizing the β distribution to minimize the discrepancy between the predictions and the observations. A constraint was applied to drive β toward a large value to avoid the flow unsteadiness owing to low eddy viscosity. The present ABDA model is expected to be applicable to various flow conditions unsolvable by simple optimizations of the model constant. This model is fully equation driven and is thus computationally cheaper than the discretized adjoint method, as well as convenient to be implemented in the existing CFD codes.

The test in the cylinder wake showed that the first-order scheme applied to the adjoint equations exhibited little effect on the final assimilation results but drove β to another solution that can also minimize the cost function. The configurations of the free jet and hump flows demonstrated the capability of the present ABDA model for the flow reproduction in shear and separation flows. The present proposed U_x-constraint strategy is more efficient for the flow assimilation than the p-constraint method previously used by others. The three-dimensional cube flow also evidenced that the present ABDA model is applicable to heavy assimilation work with a large number of grid cells.

The SA turbulence model is one of the models that can be implemented in this adjoint approach. In the present framework, the turbulence model can be also eliminated by solving directly an optimal eddy viscosity ν_t or Reynolds stress distribution rather than the correction function β. The only difference is the computational cost when the assimilation variable (ν_t, β or Reynolds stress) converges from the initial state to the optimal state. Using an appropriate turbulence model can significantly decrease this cost. The present ABDA model has been proposed only for the assimilation of steady-state flows. It minimizes the error between the assimilation result and the observations in the sense of time-averaging. It is not suitable to be applied directly in unsteady simulations. However, the unsteady version of the ABDA model can be derived according to the present procedure with the time-dependent term in both the primary and adjoint equations. We have noticed that this unsteady adjoint formulation requires much more computational efforts when integrated forward and backward in time repeatedly until convergence. Therefore, an efficient and accurate assimilation approach for unsteady flows is desired, which will be our future work.

ACKNOWLEDGMENTS

The authors gratefully acknowledge financial support for this study from the National Natural Science Foundation of China (No. 11725209).

[1]K. Duraisamy, G. Iaccarino, and H. Xiao, "Turbulence modeling in the age of data," e-print arXiv:1804.00183 (2018).
[2]K. J. H. Law, A. M. Stuart, and K. C. Zygalakis, "Data assimilation: A mathematical introduction," e-print arXiv:1506.07825 (2015).
[3]I. M. Navon, "Data assimilation for numerical weather prediction: A review," in *Data Assimilation for Atmospheric Oceanic and Hydrologic Applications* (Springer Berlin, Heidelberg, 2013), p. 21.
[4]Z. Li, H. Zhang, S. C. C. Bailey, J. B. Hoagg, and A. Martin, "A data-driven adaptive Reynolds-averaged Navier–Stokes k—ω model for turbulent flow," J. Comput. Phys. **345**, 111 (2017).
[5]H. Kato and S. Obayashi, "Statistical approach for determining parameters of a turbulence model," in *15th International Conference on Information Fusion, Singapore, 2012* (IEEE, Singapore, 2012).
[6]X. Gao, Y. Wang, N. Overton, M. Zupanski, and X. Tu, "Data-assimilated computational fluid dynamics modeling of convection-diffusion-reaction problems," J. Comput. Sci. **21**, 38 (2017).
[7]J. Larsson and G. Iaccarino, "Modeling of structural uncertainties in Reynolds-averaged Navier-Stokes closures," Phys. Fluids **25**, 110822 (2013).
[8]S. H. Cheung, T. A. Oliver, and E. E. Prudencio, "Bayesian uncertainty analysis with applications to turbulence modeling," Reliab. Eng. Syst. Saf. **96**, 1137 (2011).
[9]T. A. Oliver and R. D. Moser, "Bayesian uncertainty quantification applied to RANS turbulence models," J. Phys.: Conf. Ser. **318**, 042032 (2011).
[10]H. Xiao, J. L. Wu, J. X. Wang, R. Sun, and C. J. Roy, "Quantifying and reducing model-form uncertainties in Reynolds-averaged Navier–Stokes simulations: A data-driven, physics-informed Bayesian approach," J. Comput. Phys. **324**, 115 (2015).
[11]A. P. Singh and K. Duraisamy, "Using field inversion to quantify functional errors in turbulence closures," Phys. Fluids **28**, 045110 (2016).
[12]A. P. Singh, S. Medida, and K. Duraisamy, "Machine-learning-augmented predictive modeling of turbulent separated flows over airfoils," AIAA J. **55**, 2215 (2017).
[13]E. J. Parish and K. Duraisamy, "A paradigm for data-driven predictive modeling using field inversion and machine learning," J. Comput. Phys. **305**, 758 (2016).
[14]H. Kato, A. Yoshizawa, G. Ueno, and S. Obayashi, "A data assimilation methodology for reconstructing turbulent flows around aircraft," J. Comput. Phys. **283**, 559 (2015).
[15]M. Meldi and A. Poux, "A reduced order model based on Kalman filtering for sequential data assimilation of turbulent flows," J. Comput. Phys. **347**, 207 (2017).
[16]S. Nadarajah and A. Jameson, "A comparison of the continuous and discrete adjoint approach to automatic aerodynamic optimization," Can. J. Earth Sci. **43**, 1445 (2000).
[17]C. Othmer, "A continuous adjoint formulation for the computation of topological and surface sensitivities of ducted flows," Int. J. Numer. Methods Fluids **58**, 861 (2008).
[18]P. Spalart and S. Allmaras, "A one-equation turbulence model for aerodynamic flows," Rech. Aerosp. **1**, 5 (1994).
[19]C. He, Y. Liu, and S. Yavuzkurt, "Large-eddy simulation of circular jet mixing: Lip- and inner-ribbed nozzles," Comput. Fluids **168**, 245 (2018).
[20]D. Greenblatt, C. S. Yao, K. B. Paschal, J. Harris, N. W. Schaeffler, and A. E. Washburn, "Experimental investigation of separation control part 1: Baseline and steady suction," AIAA J. **44**, 2820 (2006).
[21]J. W. Naughton, S. A. Viken, and D. Greenblatt, "Skin friction measurements on the NASA hump model," AIAA J. **44**, 1255 (2006).
[22]R. Martinuzzi and C. Tropea, "The flow around surface-mounted prismatic obstacles placed in a fully developed channel flow," J. Fluids Eng. **115**, 85 (1993).
[23]M. Schramm, B. Stoevesandt, and J. Peinke, "Optimization of airfoils using the adjoint approach and the influence of adjoint turbulent viscosity," Computation **6**, 5 (2018).
[24]G. K. Karpouzas, E. M. Papoutsis-Kiachagias, T. Schumacher, E. de Villiers, K. C. Giannakoglou, and C. Othmer, "Adjoint optimization for vehicle external aerodynamics," Int. J. Automot. Eng. **7**, 1 (2015).
[25]L. Armijo, "Minimization of functions having Lipschitz continuous first partial derivatives," Pac. J. Math. **16**, 1 (1966).
[26]M. Lemke, *Adjoint Based Data Assimilation in Compressible Flows with Application to Pressure Determination from PIV Data* (Technische Universität Berlin, 2015).
[27]M. Meldi, "The signature of initial production mechanisms in isotropic turbulence decay," Phys. Fluids **28**, 035105 (2016).
[28]D. A. Yoder, J. R. Debonis, and N. J. Georgiadis, "Modeling of turbulent free shear flows," Comput. Fluids **117**, 212 (2015).
[29]V. Krishnan, K. D. Squires, and J. R. Forsythe, "Prediction of separated flow characteristics over a hump," AIAA J. **44**, 252 (2006).